Microstructure and Mechanical Properties of Aluminum Matrix Composites Reinforced With *In-Situ* TiB$_2$ Particles

Weiguo Wu[1], Tiancheng Zeng[1], Wenfeng Hao[2]* and Shiping Jiang[1]*

[1]Faculty of Civil Engineering and Mechanics, Jiangsu University, Zhenjiang, China, [2]College of Mechanical Engineering, Yangzhou University, Yangzhou, China

The present article investigates the microstructure and mechanical properties of A356 matrix composite reinforced with TiB$_2$ particles synthesized by the salt metal reaction of as-cast and T6 state. Microscopic observations of the prepared composites reveal that *in-situ* grown TiB$_2$ particles are characterized with regular shapes and nearly uniform distributed in the A356 matrix. A clear interface between the A356 matrix and TiB$_2$ particles was observed. The detailed analysis of mechanical properties of synthesized composites of as-cast and T6 state show that the ultimate tensile strength and Young's modulus of the synthesized composites increased with the increasing weight percentage (wt%) of *in-situ* TiB$_2$ particles in the A356 matrix, but the Poisson's ratio of the synthesized composites decreased with the increase of TiB$_2$ particles wt%. The Young's modulus of the composites increased by up to 10.8% and the Poisson's ratio decreased by up to 3.2% with the increase of TiB$_2$ particles wt%, compared to A356 alloy. With the increase of TiB$_2$ particle wt%, the yield strength of the composites decreased at first (when the TiB$_2$ particle wt% is less than 1%) then increased, while elongation and percent reduction in area increased at first and then decreased. Furthermore, T6 heat treatment can refine grain and effectively improve the mechanical properties of composites.

Keywords: *in-situ* composites, A356 alloy, TiB$_2$, microstructure, mechanical properties

INTRODUCTION

In-situ aluminum composites, which possess the advantages of small reinforcements and strong particle-matrix bonding, are studied as one of the most promising alternatives for effectively eliminating the inherent defects of *ex-situ* particulate composites (Qian et al., 2020; Raveendran et al., 2020; Pariyar et al., 2021; Zhao et al., 2021). Previous studies have also shown that *in-situ* particles can significantly enhance the mechanical properties of composites for refining the size of grain in the matrix (Afkham et al., 2018; Guan et al., 2021). In addition, Rahoma et al. (2015) studied the effect of heat treatment on the microstructure and mechanical properties of *in-situ* matrix composites and found that the ductility of matrix composites could be enhanced by increasing the aging temperatures. Kai et al. (2021) studied the effects of Zr on the microstructure and mechanical properties of B$_4$C/Al composites and pointed out that the addition of Zr could promote the wettability of the composite as well as the uniform distribution of the particles. To improve the dispersity of *in situ* particles in the matrix effectively, some external physical fields, such as electromagnetic and ultrasonic fields, were used during the preparation of the *in-situ* particle reinforced aluminum composites (Kai et al., 2016; Kai et al., 2019).

TABLE 1 | Chemical compositions of A356 alloy (wt%).

Alloy	Si	Mg	Ti	Fe	Cu	Mn	Zn	Sn	Al
A356	7.39	0.37	0.15	0.16	0.05	0.1	0.05	0.01	Bal

Al–Si based cast alloy composites (such as A356) have been widely used in automobile, aerospace, and electronics industries because of their high strength ratio and modulus ratio and better resistance to wear and corrosion (Jelinek et al., 2012; Kim et al., 2021). In order to improve the integrated properties of hypereutectic Al–Si alloys, many processing technologies have been studied to obtain superior mechanical properties. One of them is to synthesize ceramics with particle-reinforced aluminum alloy matrices by *in-situ* reactions (Tao et al., 2018; Logesh et al., 2020; Zhang et al., 2020). Among various reinforced particles, TiB$_2$ particles are one of the promising candidates because of their high hardness, high modulus, and exceptional erosion resistance (Chen et al., 2009a; Liang et al., 2019; Fattahi et al., 2020; Senthil Kumar et al., 2020). The mechanical properties and strengthening mechanisms of TiB$_2$/A356 composites have been studied by many researchers, and their reports indicate significant improvements in tensile properties (Chen et al., 2009b; Wang et al., 2014; Xue et al., 2020). Mandal et al. (2008) investigated the aging response of the alloy when dispersed with TiB$_2$ particles and observed that different amounts of TiB$_2$ alter the particle size distribution of Si, which affects the mechanical properties. Karbalaei Akbari et al. (2015) indicated that the tensile properties of nanocomposites were evidently different from the enhancement of microparticles. Zulkamal et al. (2018) reported that the addition of TiB$_2$ particles refined the microstructure of the material and improved the wear resistance of the semi-solid A356 alloy. Deepak et al. (2019) have conducted low cycle fatigue tests on *in-situ* TiB$_2$/A356 composites and found that TiB$_2$ particles had a significant impact on the structure, hardness, tensile strength, and fatigue life of the composites.
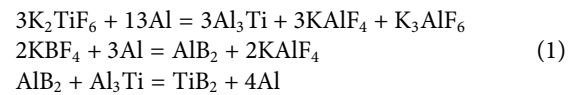
Our review of the literature indicates that limited information is available on the integrated mechanical properties of A356 matrix composite reinforced with *in-situ* grown TiB$_2$ particles. Although some research works exist on the yield strength, ultimate tensile strength, and wear of composites, reports on the Poisson's ratio of TiB$_2$/A356 *in-situ* composites are still lacking. Therefore, in this work, the A356 matrix composites reinforced with *in-situ* grown TiB$_2$ particles were synthesized by salt–metal reaction. An attempt is to study the microstructure and mechanical properties of composites of as-cast and T6 state as detailed as possible.

MATERIALS AND METHODS

Materials
The raw materials that were used in the present work are commercial A356 alloy, inorganic salt KBF$_4$ (KBF$_4$ $\geq$ 99.80%, Fe$_2$O$_3$ $\leq$ 0.05, H$_2$O $\leq$ 0.15) and K$_2$TiF$_6$ (K$_2$TiF$_6$ $\geq$ 99.80%, Fe$_2$O$_3$ $\leq$ 0.05, H$_2$O $\leq$ 0.15) powders. The chemical composition of A356 alloy is shown in **Table 1**. *In-situ* endogenous TiB$_2$ particles were

synthesized as reinforcing phase, and physical properties were shown in **Table 2**. The formation of the TiB$_2$ particles in the inorganic salt melt is given by the following chemical reactions (Bartels et al., 1997):

$$3K_2TiF_6 + 13Al = 3Al_3Ti + 3KAlF_4 + K_3AlF_6$$
$$2KBF_4 + 3Al = AlB_2 + 2KAlF_4 \qquad (1)$$
$$AlB_2 + Al_3Ti = TiB_2 + 4Al$$

Processing of TiB$_2$/A356 *In-Situ* Composites
The TiB$_2$/A356 *in-situ* composites were prepared by the inorganic salt metal reaction technique. The required KBF$_4$ and K$_2$TiF$_6$ halide salt was strictly mixed uniform in a grinding bowl according to the mass ratio Ti: B = 1:2, and was preheated to 300°C for 3 h in an electric furnace to remove moisture content. The A356 alloy and pure aluminum were heated to 800°C in a graphite crucible inside an electric furnace under nitrogen gas protection and stirred mechanically with a speed of 500 r/min. The ready-mixed KBF$_4$ and K$_2$TiF$_6$ powders were added and pressed into the melt and underwent a chemical reaction with the melt to synthesize TiB$_2$ particles. In the reaction process, the melt was still stirred for 10 min to distribute the TiB$_2$ particles. After a reaction time of half an hour, the composites melt was degassed, dross-decanted and refined, and then set for 10 min at 720°C. Finally, the composites melt was poured into a preheated copper mold, and cooled at room temperature to obtain the as-cast composites.

Each prepared TiB$_2$/A356 *in-situ* composite ingot (wt% of TiB$_2$ particles are 0%, 1%, 3%, and 5% respectively) was sectioned into two parts. One part was conducted T6 heat treatment with following steps: the composites ingot were first heated to 550°C and solution treatment for 12 h, then water quenching, finally aging treatment for 2 h at 120°C and aging treatment for 8 h at 150°C. Some composites feedstock of as-cast and T6 state were machined into the testing specimens with dimensions 10 mm × 10 mm × 10 mm. The testing surface of the specimen was carefully polished until the surface was clear and clean.

MICROSTRUCTURAL CHARACTERIZATIONS
The microstructures of the A356 alloy and TiB$_2$/A356 *in-situ* composites were characterized using an optical microscope and scanning electron microscope (JSM-7001F) with energy dispersive X-ray (EDX). **Figure 1** shows optical micrographs of the A356 alloy and 3wt% TiB$_2$ composites of as-cast. From **Figure 1A**, it can be seen that the microstructures of as-cast A356 alloy show a dendritic structure. But the addition of TiB$_2$ particles refines the structure of the dendrites as shown in **Figure 1B**. And it is also found that the TiB$_2$ particles decrease the size of needles Si to finer size in composites compared with that of A356 alloy. This suggests that TiB$_2$ particles have the effect of refining grain, as reported in earlier papers (Wang et al., 2014; Liang et al., 2019).

TABLE 2 | Properties of ceramic particles TiB$_2$.

Ceramic particle	Density (×10^3 kg/m^3)	Coefficient of thermal expansion (10^{-6}°C^{-1})	Young's modulus (GPa)	Poisson's ratio
TiB$_2$	4.50	8.28	569	0.11
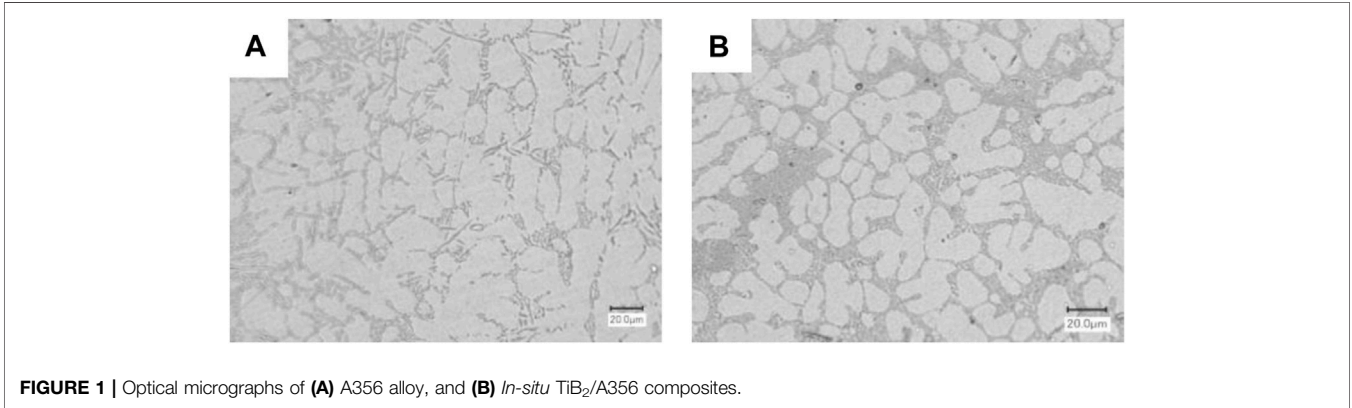
FIGURE 1 | Optical micrographs of **(A)** A356 alloy, and **(B)** *In-situ* TiB$_2$/A356 composites.
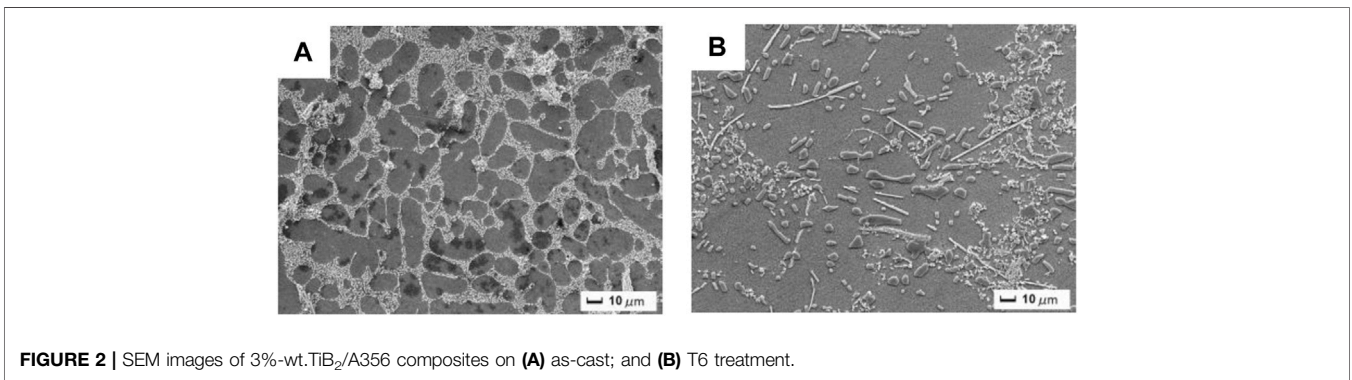
FIGURE 2 | SEM images of 3%-wt.TiB$_2$/A356 composites on **(A)** as-cast; and **(B)** T6 treatment.
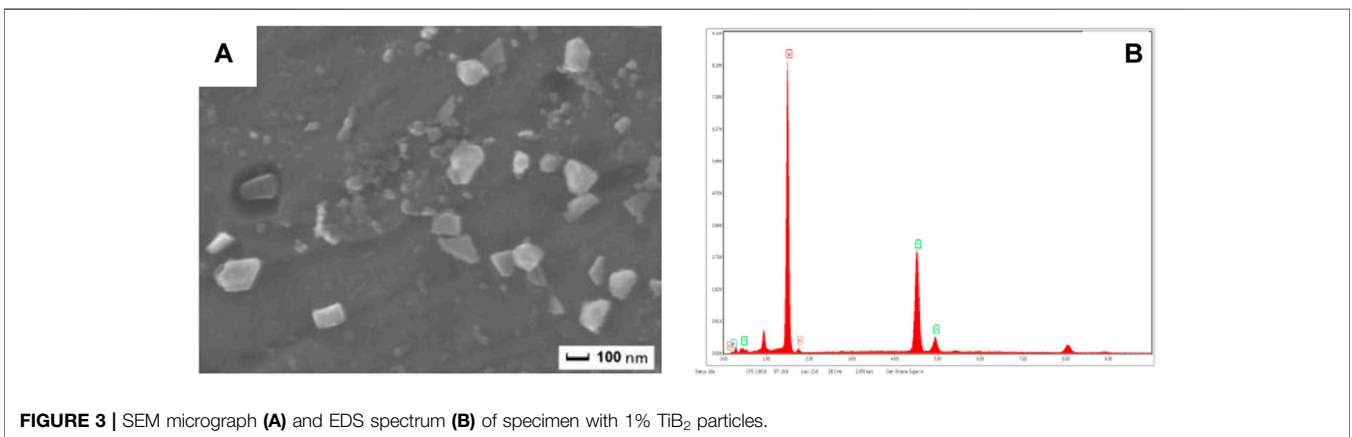
FIGURE 3 | SEM micrograph **(A)** and EDS spectrum **(B)** of specimen with 1% TiB$_2$ particles.

Further, SEM photomicrographs were taken to analyze the effect of TiB$_2$ particles in the matrix after T6 heat treatment. **Figure 2** shows SEM photos of the prepared composite of as-cast and T6 state, respectively. The microstructure of composites in **Figure 2B** shows that the dendritic eutectic Si grains were broken and spheroidised after T6 heat treatment. TiB$_2$ particles are
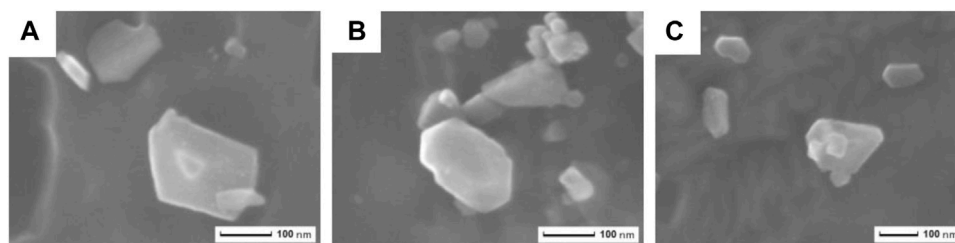
FIGURE 4 | SEM images of TiB$_2$ particles at higher magnification (A) region 1 (B) region 2 (C) region 3.
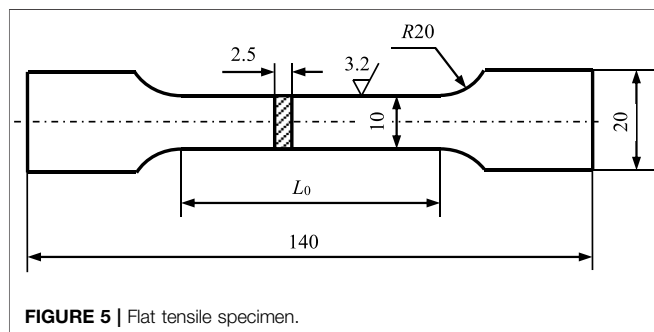

FIGURE 5 | Flat tensile specimen.

distributed on the boundaries of grains which may refine the eutectic silicon and cause an increase in mechanical properties of composites compared with those of the matrix.

The composition of the prepared composites was identified using energy dispersion spectrum (EDS) analysis. **Figure 3** shows the SEM micrograph and EDS of the A356–1wt% TiB$_2$ composites. As shown in **Figure 3B**, the EDS peaks for TiB$_2$ particles include compositional information of Ti and B except the Al matrix around the particles. And Ti and B peaks correspond to the composition of TiB$_2$ particles. This suggests that the TiB$_2$ particles were successfully synthesized in composite by *in-situ* salt metal reactions.

Figure 3A SEM micrograph reveals the size and distribution of *in-situ* grown TiB$_2$ particles inside the composites of as-cast. It is observed that most of the *in-situ* grown TiB$_2$ particles have a size of about 50–300 nm and are distributed nearly uniformly in the matrix. This contributes to the better mechanical properties of the composites. The SEM images of TiB$_2$ particles at higher magnification are shown in **Figure 4**, and it is evident that *in-situ* grown TiB$_2$ particles present regular shapes such as ellipsoids, quadrangles, and pentagons. In addition, the clean interface between the TiB$_2$ particles and A356 alloy can be observed. which is needed to enhance the mechanical properties and increase the load carrying capability of composites.

TENSILE TESTING

Equipment and Specimen

The type of specimen used in the tensile test is shown in **Figure 5**. The cross-sectional area of the flat tensile specimen has been

accurately determined as 10 mm × 2.5 mm and the length between two gage marks on the specimen is a distance L_0 = 57 mm. The tensile tests were conducted using a universal testing machine at room temperature. Before the formal test, each specimen is preloaded to 30 MPa (elastic limit is more than 40 MPa) and unloaded. Then the formal tensile test was conducted with loading speed controlled by displacement of 0.1 mm/min in the elastic stage. This kind of test was repeated at least three times on average to determine the Young's modulus Poisson's ratio of the composites. After the elasticity stage, the loading speed rate was set as 0.3 mm/min until the specimen fractured. From the stress-strain diagram recorded by the computer according to the load-displacement data, one can measure and determine the yield strength, ultimate tensile strength, percent elongation, and percent reduction in area of the composites. Each value of tensile properties is an average of at least three specimens.

Mechanical Properties

Young's modulus and Poisson's ratio are fundamental mechanical parameters of composites and involve only the straight-line segment of the stress-strain diagram of tensile tests. The normal stress σ is proportional to the strain ε as Hooke's law

$$\sigma = E\varepsilon \tag{2}$$

Where the stress σ can be calculated using the applied load, and strain ε can be read directly using an electrical-resistance strain gage. Then Young's modulus E can be determined by **Eq. 2**. Poisson's ratio υ characterizes the ratio between the lateral strain ε' and longitudinal strain ε of material under tensile load within the elastic range.

$$\upsilon = \left| \frac{\varepsilon'}{\varepsilon} \right| \tag{3}$$

To measure the lateral strain and longitudinal strain of composites under the tensile load, the electrical strain gages were pasted at the surface of the specimen before testing, as shown in **Figure 6A**. On one side surface, two pieces of electrical strain gage were pasted lateral and longitudinal respectively, while two pieces of electrical strain gage were pasted at the same position on another side surface of the specimen. The full-bridge connection scheme in **Figure 6B** is used to eliminate the influence of initial bend and eccentric loading that may exist
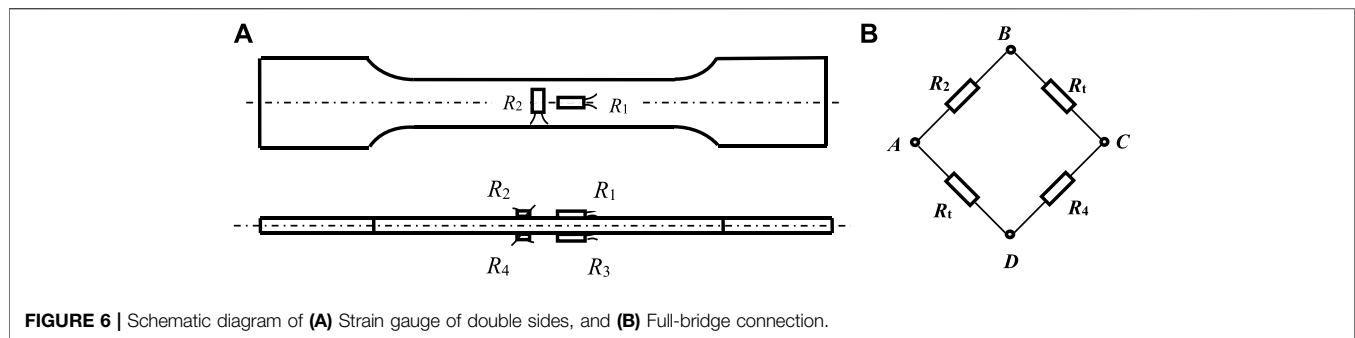
FIGURE 6 | Schematic diagram of **(A)** Strain gauge of double sides, and **(B)** Full-bridge connection.

in the process of testing, and improve the measurement precision of the Poisson's ratio. Then the strain formula read by the strain gauge is as follows:

$$
\begin{aligned}
\varepsilon_{ds} &= \varepsilon_1 - \varepsilon_2 + \varepsilon_3 - \varepsilon_4 \\
&= (\varepsilon_T + \varepsilon_W + \varepsilon_{t1}) - \varepsilon_{t1} + (\varepsilon_T - \varepsilon_W + \varepsilon_{t2}) - \varepsilon_{t2} \\
&= 2\varepsilon_T
\end{aligned}
\tag{4}
$$

where ε_{ds} is strain of the strain gauge, ε_t is the strain caused by temperature variation, ε_w is bending strain of specimen, ε_T is the strain of axial or lateral under the load.

The TiB$_2$/A356 *in-situ* composites have no obvious yield stage in the stress-strain diagram, but also show certain plastic characteristics. Therefore, the yield strength $\sigma_{0.2}$ was used, which is obtained by drawing a line parallel to the straight-line segment of the stress-strain diagram through the point with the abscissa $\varepsilon = 0.2\%$. As the load increases, the specimen eventually breaks, and the largest force is reached. The stress corresponding to this largest force is denoted by the ultimate tensile strength (UTS) σ_b.

The ductility of composites is characterized by its percent elongation δ

$$
\delta = \frac{L_1 - L_0}{L_0} \times 100\%
\tag{5}
$$

Where, L_0 and L_1 denote the initial length of the specimen and its final length after rupture, respectively. Another measure of ductility is the percent reduction in area Ψ

$$
\psi = \frac{A - A_1}{A} \times 100\%
\tag{6}
$$

Where, A_0 and A_1 denote the initial cross-sectional area of the specimen and its minimum cross-sectional area after rupture, respectively.

RESULTS AND DISCUSSION

Young's Modulus and Poisson's Ratio

Figure 7 shows the variation of Young's modulus and Poisson's ratio of the prepared composites as a function of weight percentage (wt%) of TiB$_2$ particles. A obvious enhancement is observed in Young's modulus of the composites comparing with that of the non-reinforced A356 alloy, and the increase is nearly linear with the increasing wt% of TiB$_2$ particles of as-cast and T6 state. The average Young's modulus of composites of T6 state with TiB$_2$ particles wt% of 1%, 3%, and 5% increase by 3.02%, 8.08%, and 10.87% respectively, compared with A356 alloys. Therefore, the addition of high modulus particles is one of the most effective methods to improve the Young's modulus of composites. From **Figure 7A**, it is also found that T6 heat treatment can increase the Young's modulus of composites by a small amount, which increases to a maximum of 1.76% compared with the as-cast composites of 5 wt% TiB$_2$. This is attributed to the fact that Young's modulus characterizes the overall performance of the composites and is determined by atomic nature of metal and lattice type, with less influence from grain size and second phase dispersion. That is, the Young's modulus of composites is insensitive to the variation of the microstructure caused by the T6 heat treatment.

Figure 7B shows the influence on Poisson's ratio of the prepared composites with increasing of wt% of TiB$_2$ particles. It can be observed that the addition of TiB$_2$ to the A356 alloy decreased the Poisson's ratio of composites of as-cast and T6 treatment. The average Poisson's ratio of composites with wt% of TiB$_2$ particles of 1%, 3%, and 5% decreased to about 1.20%, 1.92%, and 3.18%, respectively, compared to that of A356 alloy. This is because the Poisson's ratio of A356 alloy is 0.321 and the Poisson's ratio of TiB$_2$ particles is 0.11, and the presence of hard TiB$_2$ particles influences the elastic deformation of composites. Therefore, with the increase of TiB$_2$ particles, the Poisson's ratio of composites shows a decreasing trend. From **Figure 7B**, it can be found that microstructural variation occurring at higher processing temperatures influences the Poisson's ratio slightly. The average Poisson's ratio of composites with TiB$_2$ particles of 1%, 3%, and 5% in T6 state decreases by 0.6%, 0.73%, and 1.22%, respectively, compared to that of composite in as-cast.

Yield Strength and Ultimate Tensile Strength

The effect of wt% of TiB$_2$ particles on the yield strength and ultimate tensile strength of the prepared composites is presented in **Figure 8**. It shows that the yield strength and ultimate tensile strength of composites of as-cast and T6 state increased with the increase of wt% of TiB$_2$ particles. The enhancement in tensile strength of composites is the synthetic effect of various parameters that affect the mechanical properties of
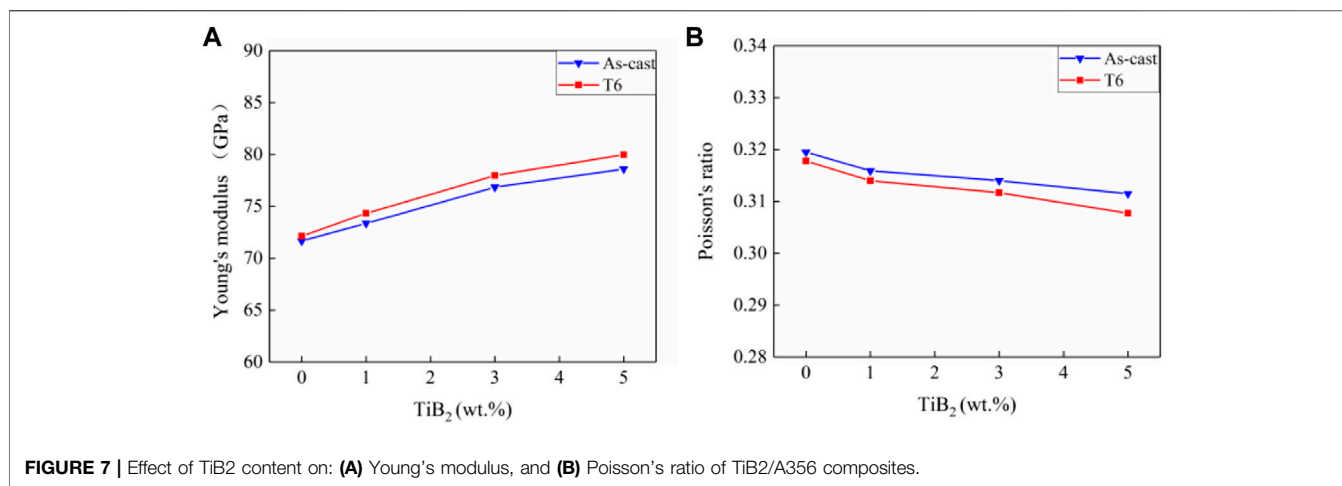
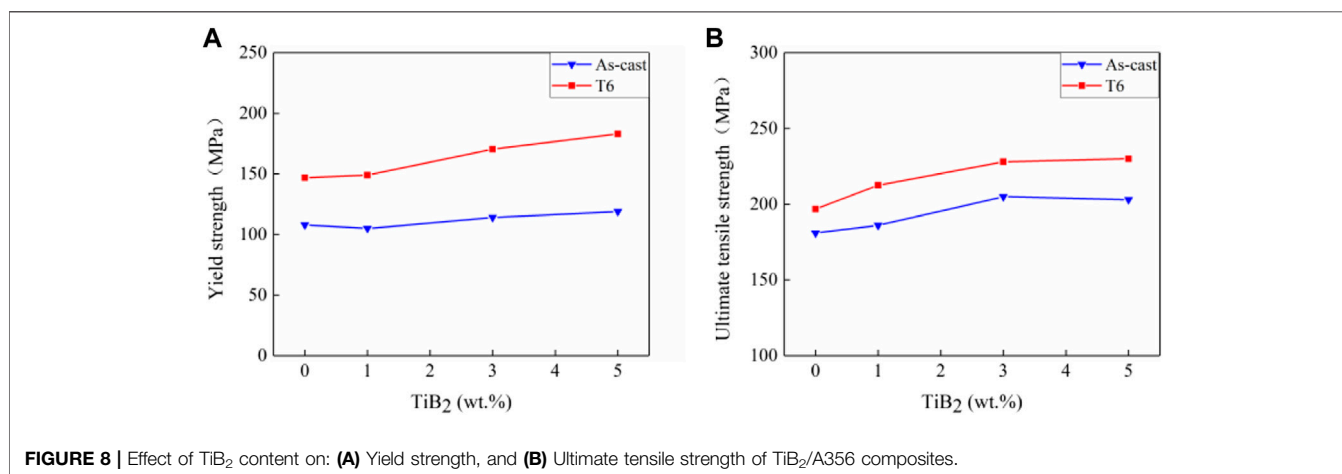**FIGURE 7 |** Effect of TiB2 content on: **(A)** Young's modulus, and **(B)** Poisson's ratio of TiB2/A356 composites.

FIGURE 8 | Effect of TiB$_2$ content on: **(A)** Yield strength, and **(B)** Ultimate tensile strength of TiB$_2$/A356 composites.

composites. The grain refinement and strong thermal stress at TiB$_2$/A356 interface because of the difference in the thermal expansion coefficient of A356 alloys and TiB$_2$ particles are important reasons to increase the strength of composites. A well bonded and clean interface leads to the transfer of tensile load from the A356 matrix to the distributed TiB$_2$ particles effectively, and is also a reason for the increasing tensile strength of composites. From the figure, it also can be found that the average yield strength and ultimate tensile strength of composites of T6 state are much greater than that of as-cast composites. One of the reasons is that T6 heat treatment can effectively improve the microstructure of composite as analyzed in *Microstructural Characterizations*. Which causes the enhancement of tensile strength of composites.

It is noted from **Figure 8A** that when the wt% of TiB$_2$ particles is less than 1%, the yield strength of the composites does not increase significantly, and is less than that of A356 alloy. This is because the addition of reinforced particles can enhance the strength of the A356 matrix, but the presence of reinforced particles will also damage the continuity of the matrix alloy to a certain extent, and even form microporosity which is known as a defect in the matrix. Therefore, the strengthening and

weakening factors of mechanical properties of composites offset the effects of each other, and thus, with less wt% of TiB$_2$ particles (in this work, less than 1 wt%), the reinforcement degree of the particles is not enough to offset the weakening factors in the matrix structure. However, with the increasing of the wt% of TiB$_2$ particles to a critical value, the strengthening effect of particles on A356 alloy is greter than the weakening factors in the matrix structure, and the yield strength of the composites shows an increasing trend with the increasing of wt% of TiB$_2$ particles.

Figure 8B shows that the ultimate tensile strength of the prepared composites increases with the increase of the wt% of TiB$_2$ particles, but further increase of *in-situ* TiB$_2$ particle content (in this work, more than 5 wt%) leads to the reduction in the ultimate tensile strength of the composites. This is because, in contrast to the elastic property of composites, ultimate tensile strength characterizes the local performance of composites and is more sensitive to various defects inside composites. In the preparation of *in-situ* TiB$_2$/A356 composites, it is inevitable to cause an amount of porosity, particle clusters, and slag inclusion, which result in stress concentration and micro-cracks are likely to occur in the periphery with small load. **Figure 9** shows the
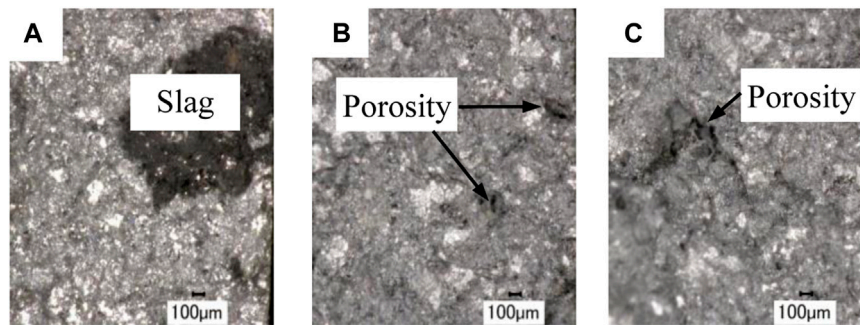
FIGURE 9 | Defects inside the TiB$_2$/A356 composites **(A)** region 1 **(B)** region 2 **(C)** region 3.
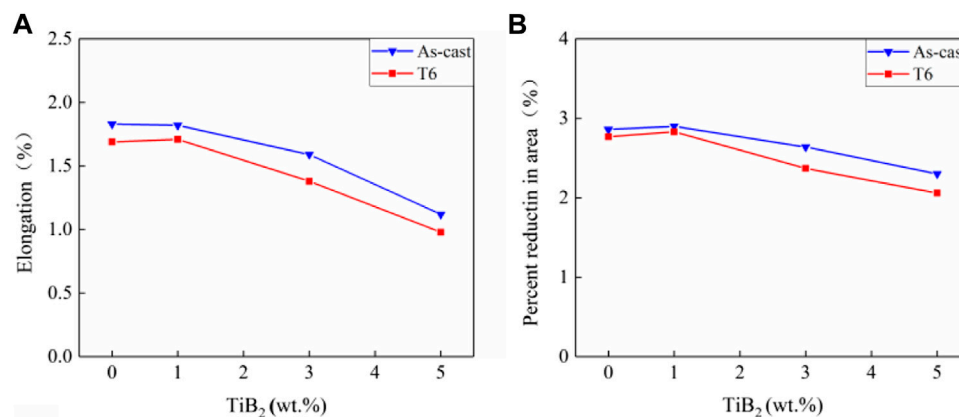

FIGURE 10 | Effect of TiB$_2$ content on: **(A)** Percent elongation, and **(B)** Percent reduction in area of TiB$_2$/A356 composites.

fracture photos of the specimen with low tensile strength (particles 5 wt%). It can be seen that there is slag inclusion of reaction residues, pores, and porosity of different sizes inside the composites. These defects reduce the tensile strength of the composites to a certain extent. Another reason is that the increasing wt% of TiB$_2$ particles increased the viscosity of the halide melt, which reduces the fluidity of the A356 melt and reduces the diffusion of reactants, which leads to difficulty in the chemical reaction and casting molding. Therefore, higher wt% of TiB$_2$ particles would weaken the enhancement effect of the composites. Wood et al. (Chen et al., 2009a) reported that the volume fraction of *in-situ* synthesized particles should not be higher than 12% to ensure the good fluidity of the composites and the final casting forming.

Elongation and Percent Reduction in Area

Figure 10 show the elongation of the prepared composites of as-cast and T6 state and the percent reduction in area (PRA) for different wt% of TiB$_2$ particles. It can be seen that with the increasing wt% of TiB$_2$ particles, the elongation and percent reduction in area of the composites increase at first (wt% of TiB$_2$ particles less than 1%) and then decrease on both as-cast and T6 state. The elongation of composites decreased to a maximum

of 38.7%, and the percent reduction in area decreased by about 19.6% when adding 5 wt% TiB$_2$ particles to the A356 alloy. On the one hand, the presence of hard TiB$_2$ particles decreases the ductility of composites; on the other, the presence of TiB$_2$ particles can refine the grain of composites, and grain refinement improves not only the strength but also the plasticity and toughness of the composites because when there are more grains in a certain volume, the deformation is borne by more grains. Therefore, the *in-situ* TiB$_2$/A356 composites can endure large plastic deformation, showing good ductility. Within less wt% of TiB$_2$ particles, the improvement degree of the ductility offset the brittleness of the matrix, which leads to an increase in the elongation and percent reduction in area of the composites with the increase of TiB$_2$ particles up to 1 wt%. Once the improvement of ductility is not enough to offset the increase of brittleness, the elongation and percent reduction in area of the composite show a decreasing trend with the increasing wt% of TiB$_2$ particles.

Fracture Behavior

Figure 11A shows the photos of the specimen of the prepared composite after fracturing at room temperature. It can be seen that the deformation of the specimen is tiny without an obvious
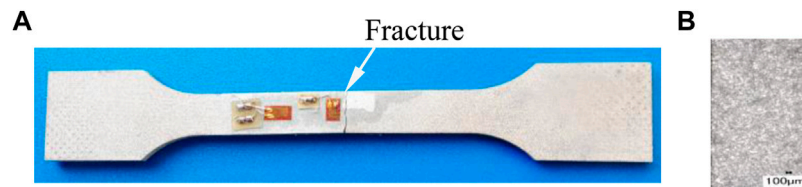
FIGURE 11 | Fracture of specimen after rupture **(A)** photo of specimen **(B)** fracture surface.
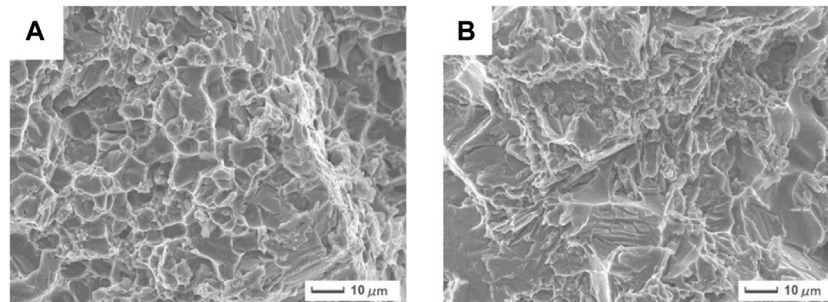

FIGURE 12 | The SEM fractographs of the fracture of TiB$_2$/A356 *in-situ* composites on **(A)** as-cast and **(B)** T6 treatment.

necking phenomenon on the fracture surface, and the fracture surface is relatively flat and nearly vertical to the tensile stress. The fracture morphology with 100 times magnified view in **Figure 11B** reveals the glossy crystalline bright surface. These phenomena show the characteristics of brittle fracture.

The fracture SEM morphology of the prepared composites is presented in **Figure 12**, which shows that there are many uniformly distributed voids with different sizes and tear edges on the tensile fracture of the composites. The larger voids lead to ductile fractures, while smaller size voids cause brittle fracture macroscopical and ductile fracture microscopical. This contributes to the debonding of the interface between the TiB$_2$ particles and A356 matrix under the action of external load, which is easy to induce crack initiation and expand along the interface to form voids. The voids gradually grow up with the deformation process and expand rapidly once passing through the interface, which leads to the final fracture of the composites.

CONCLUSION

In the present study, A356 alloy reinforced with various wt% (0, 1%, 3%, and 5%) of TiB$_2$ particles were prepared by the reaction of KBF$_4$ and K$_2$TiF$_6$ with melted aluminum. The *in-situ* grown TiB$_2$ particles were characterized with regular shapes and nearly uniformly distributed in the alloy matrix. A clear interface and good interface bonding between the A356 matrix and TiB$_2$ particles was achieved. The mechanical properties of the prepared composites of as-cast and T6 state were studied with an axial tensile test and the strain electrical measurement method. A great enhancement in tensile properties is obtained compared

with those of the non-reinforced A356 alloys. As the proportion of TiB$_2$ particles increases, the Young's modulus and ultimate tensile strength of the composites increase, while the Poisson's ratio of the composites decreases. The yield strength of the composites decreases at first (when particle wt% is less than 1%) then increases, while elongation and percent reduction in area increase at first and then decrease with the increasing wt% of TiB$_2$ particles. T6 heat treatment can refine the grain and effectively improve the mechanical properties of TiB$_2$/A356 *in-situ* composites.

DATA AVAILABILITY STATEMENT

The raw data supporting the conclusion of this article will be made available by the authors, without undue reservation.

AUTHOR CONTRIBUTIONS

WW: Data curation; Roles/Writing—original draft TZ: Data curation; Formal analysis WH: Investigation; Methodology; Project administration; SJ: Writing—review and editing; Supervision.

FUNDING

REFERENCES

Afkham, Y., Khosroshahi, R. A., Rahimpour, S., Aavani, C., Brabazon, D., and Mousavian, R. T. (2018). Enhanced Mechanical Properties of *In Situ* Aluminium Matrix Composites Reinforced by Alumina Nanoparticles. *Arch. Civil Mech. Eng.* 18 (1), 215–226. doi:10.1016/j.acme.2017.06.011

Bartels, C., Raabe, D., Gottstein, G., and Huber, U. (1997). Investigation of the Precipitation Kinetics in an Al6061/TiB2 Metal Matrix Composite. *Mater. Sci. Eng. A* 237 (1), 12–23. doi:10.1016/s0921-5093(97)00104-4

Chen, X. W., Pei, G. L., and Jin, Y. S. (2009a). Study on Accelerated Ageing of Aeronautical Perspex(PMMA) in Ultraviolet. *J. Aeronaut. Mater.* 29, 107–112. doi:10.3969/j.issn.1005-5053.2009.6.022

Chen, X. W., Zhang, T. J., and Liu, S. H. (2009b). Accelerated Ageing Behavior of PMMA under Hygrothermal Air and Water Conditions. *Fail. Anal. Prev.* 4, 193–195. doi:10.3969/j.issn.1673-6214.2009.04.001

Deepak, S., Jha, S. K., Karthik, D., and Mandal, A. (2019). Fatigue Analysis of A356-TiB$_2$ (5wt%) *In-Situ* Nano Composites. *Mater. Today-Proceedings* 18 (3), þ774–779. doi:10.1016/j.matpr.2019.06.494

Fattahi, M., Pazhouhanfar, Y., Delbari, S. A., Shaddel, S., Namini, A. S., and Shahedi Asl, M. (2020). Influence of TiB2 Content on the Properties of TiC-SiCw Composites. *Ceramics Int.* 46 (6), 7403–7412. doi:10.1016/j.ceramint.2019.11.236

Guan, C., Zhao, Y., Chen, G., Kai, X., Qian, W., Tao, R., et al. (2021). Synergistic Strengthening and Toughening of Copper Coated Graphene Nanoplates and *In Situ* Nanoparticles Reinforced AA6111 Composites. *Mater. Sci. Eng. A* 822, 141661. doi:10.1016/j.msea.2021.141661

Jelinek, B., Groh, S., and Horistemeyer, M. F. (2012). Modified Embedded Atom Method Potential for Al, Si, Mg, Cu, and Fe Alloys. *Phys. Rev. B* 85 (24), 5102–5113. doi:10.1103/physrevb.85.245102

Kai, X., Huang, S., Wu, L., Tao, R., Peng, Y., Mao, Z., et al. (2019). High Strength and High Creep Resistant ZrB2/Al Nanocomposites Fabricated by Ultrasonic-Chemical *In-Situ* Reaction. *J. Mater. Sci. Technol.* 35, 2107–2114. doi:10.1016/j.jmst.2019.04.020

Kai, X., Tian, K., Wang, C., Jiao, L., Chen, G., and Zhao, Y. (2016). Effects of Ultrasonic Vibration on the Microstructure and Tensile Properties of the Nano ZrB2/2024Al Composites Synthesized by Direct Melt Reaction. *J. Alloys Compd.* 668, 121–127. doi:10.1016/j.jallcom.2016.01.152

Kai, X., Wu, L., Peng, Y., Tan, Z., Li, G., Chen, G., et al. (2021). Effects of Zr Element on the Microstructure and Mechanical Properties of B4C/Al Composites Fabricated by Melt Stirring Method. *Composites B: Eng.* 224, 109156. doi:10.1016/j.compositesb.2021.109156

Karbalaei Akbari, M., Baharvandi, H. R., and Shirvanimoghaddam, K. (2015). Tensile and Fracture Behavior of Nano/micro TiB2 Particle Reinforced Casting A356 Aluminum alloy Composites. *Mater. Des. (1980-2015)* 66, 150–161. doi:10.1016/j.matdes.2014.10.048

Kim, S-W., Lee, S-J., Dae-Up, K., and Kim, M-S. (2021). Experimental Investigation on Tensile Properties and Yield Strength Modeling of T5 Heat-Treated Counter Pressure Cast A356 Aluminum Alloys. *Metals* 11, 1–17. doi:10.3390/met11081192

Liang, Z., Zhang, S.-L., Guan, C., Yin, H., Zhenya, Z., Wu, J.-L., et al. (2019). Effects of Rolling on Microstructures and Properties of *In-Situ* (TiB2 + ZrB2)/AlSi9Cu1 Composites. *Mater. Res. Express* 6 (10), 106584. doi:10.1088/2053-1591/ab3b36

Logesh, K., Hariharasakthisudhan, P., Arul Marcel Moshi, A., Rajan, B. S., and K, S. (2020). Mechanical Properties and Microstructure of A356 alloy Reinforced AlN/MWCNT/graphite/Al Composites Fabricated by Stir Casting. *Mater. Res. Express* 7 (1), 015004. doi:10.1088/2053-1591/ab587d

Mandal, A., Chakraborty, M., and Murty, B. S. (2008). Ageing Behaviour of A356 alloy Reinforced with *In-Situ* Formed TiB2 Particles. *Mater. Sci. Eng. A* 489, 220–226. doi:10.1016/j.msea.2008.01.042

Pariyar, A., Perugu, C. S., Toth, L. S., and Kailas, S. V. (2021). Microstructure and Mechanical Behavior of Polymer-Derived *In-Situ* Ceramic Reinforced Lightweight Aluminum Matrix Composite. *J. Alloys Compd.* 880, 160430. doi:10.1016/j.jallcom.2021.160430

Qian, W., Zhao, Y., Kai, X., Yan, Y., Gao, X., and Jin, L. (2020). Microstructure and Properties of 6111Al Matrix Composites Reinforced by the Cooperation of *In Situ* ZrB2 Particles and Y. *J. Alloys Compd.* 829, 154624. doi:10.1016/j.jallcom.2020.154624

Rahoma, H. K. S., Wang, X. P., Kong, F. T., Chen, Y. Y., Han, J. C., and Derradji, M. (2015). Effect of (α+β) Heat Treatment on Microstructure and Mechanical Properties of (TiB+TiC)/Ti-B20 Matrix Composite. *Mater. Des.* 87, 488–494. doi:10.1016/j.matdes.2015.08.028

Raveendran, S., Alam, M. M., Khan, M. I. K., Dhayalan, A., and Kannan, S. (2020). *In Situ* formation, Structural, Mechanical and *In Vitro* Analysis of ZrO2/ZnFe2O4 Composite with Assorted Composition Ratios. *Mater. Sci. Eng. C* 108, 110504. doi:10.1016/j.msec.2019.110504

Senthil Kumar, P., Kavimani, V., Soorya Prakash, K., Murali Krishna, V., and Shanthos Kumar, G. (2020). Effect of TiB2 on the Corrosion Resistance Behavior of *In Situ* Al Composites. *Inter. Metalcast.* 14 (1), 84–91. doi:10.1007/s40962-019-00330-3

Tao, R., Zhao, Y., Kai, X., Wang, Y., Qian, W., Yang, Y., et al. (2018). The Effects of Er Addition on the Microstructure and Properties of an *In Situ* Nano ZrB2-Reinforced A356.2 Composite. *J. Alloys Compd.* 731, 200–209. doi:10.1016/j.jallcom.2017.10.021

Wang, M., Chen, D., Chen, Z., Wu, Y., Wang, F., Ma, N., et al. (2014). Mechanical Properties of *In-Situ* TiB2/A356 Composites. *Mater. Sci. Eng. A* 590, 246–254. doi:10.1016/j.msea.2013.10.021

Xue, J., Wu, W., Ma, J., Huang, H., and Zhao, Z. (2020). Study on the Effect of CeO2 for Fabricating *In-Situ* TiB2/A356 Composites with Improved Mechanical Properties. *Mater. Sci. Eng. A* 786, 139416. doi:10.1016/j.msea.2020.139416

Zhang, H., Chen, G., Zhang, Z., Zhao, Y., Mu, S., Xu, J., et al. (2020). Study on the Grain Refinement of A356 alloy by Al-3wt-% VN Master alloy. *Mater. Sci. Technol.* 36 (7), 819–826. doi:10.1080/02670836.2020.1743925

Zhao, Z., Wang, S., Du, W., Bai, P., Zhang, Z., Wang, L., et al. (2021). Interfacial Structures and Strengthening Mechanisms of *In Situ* Synthesized TiC Reinforced Ti6Al4V Composites by Selective Laser Melting. *Ceramics Int.* 47 (24), 34127–34136. doi:10.1016/j.ceramint.2021.08.323

Zulkamal, N. A. M., Nasir, L. M. M., and Anasyida, A. S. (2018). Microstructure and Wear Properties of T6 Heat Treated Semisolid A356-TiB2 Composite. *J. Phys. Conf. Ser.* 1082, 012065. doi:10.1088/1742-6596/1082/1/012065